CONDENSED MATTER PHYSICS

Real-space imaging and control of chiral anomaly induced current at room temperature in topological Dirac semimetal

Byung Cheol Park[1]†, Taewoo Ha[2]†, Kyung Ik Sim[2], Taek Sun Jung[3], Jae Hoon Kim[3], Yeongkwan Kim[4], Young Hee Lee[1,2], Teun-Teun Kim[5], Sung Wng Kim[1,2]*

Chiral fermions (CFs) in condensed matters, distinguished by right (+) or left (−) handedness, hold a promise for emergent quantum devices. Although a chiral anomaly induced current, $J_{chiral} = J(+) - J(-)$, occurs in Weyl semimetals due to the charge imbalance of the CFs, monitoring spatial flow and temporal dynamics of J_{chiral} has not been demonstrated yet. Here, we report real-space imaging and control of J_{chiral} on the topological Dirac semimetal KZnBi at room temperature (RT) by near-field terahertz (THz) spectroscopy, establishing a relation for an electromagnetic control of J_{chiral}. In THz electric and external magnetic fields, we visualize a spatial flow of coherent J_{chiral} in macroscopic length scale and monitor its temporal dynamics in picosecond time scale, revealing its ultralong transport length around 100 micrometers. Such coherent J_{chiral} is further found to be controlled according to field directions, suggesting the feasibility of information science with topological Dirac semimetals at RT.

INTRODUCTION

Three-dimensional (3D) topological semimetal is an exotic quantum phase, called as a 3D analog of graphene, providing a platform for studying Weyl physics of the chiral fermions (CFs) (*1*–*3*). Chiral anomaly, a nonconservation of the CFs, is a representative phenomenon in topological semimetals. To date, low-temperature magneto-transport studies on topological Dirac and Weyl semimetals have proved the presence of the chiral anomaly induced CFs (*3*–*10*) in momentum space with a band structure and its chemical potential shift (*3*–*10*). Considering that the chiral anomaly induced CFs are topologically protected in real space, their charge flow, $\boldsymbol{J}_{chiral}$, can inevitably appear in the samples of topological semimetals at room temperature (RT) and give clear experimental evidence on the proposed chiral anomaly induced real-space phenomena such as the chiral separation effect (*11*, *12*), chiral electric separation (*11*, *13*), and viscous and vortical hydrodynamic flow of CFs (*11*, *14*–*16*). However, although many transport measurements have attempted to substantiate real-space chiral anomaly (*17*, *18*), the real-space imaging of $\boldsymbol{J}_{chiral}$ and RT chiral anomaly induced $\boldsymbol{J}_{chiral}$ has not been demonstrated yet.

Beyond the imaging of chiral anomaly induced CFs and $\boldsymbol{J}_{chiral}$, controlling a dissipationless $\boldsymbol{J}_{chiral}$ with electromagnetic fields in topological materials can be a potential approach to demonstrate next-generation information technology. Quantifying the temporal and spatial dynamics of the CFs is a prerequisite to manipulating the $\boldsymbol{J}_{chiral}$ in real space. Because the CFs can be regarded as collective plasma and induced by electromagnetic waves, measuring their oscillatory motion and AC current flow in temporal and spatial domains allows visualizing and controlling the $\boldsymbol{J}_{chiral}$ in a practical way at easily accessible temperatures. Here, by establishing the electrodynamic principle for the CF plasma with the near-field terahertz (THz) spectroscopy, we succeed in visualizing the flow of real-space $\boldsymbol{J}_{chiral}$ at RT and further present the controllability of the $\boldsymbol{J}_{chiral}$ plume in spacetime.

RESULTS AND DISCUSSION

Figure 1 illustrates the means of generating $\boldsymbol{J}_{chiral}$ in a 3D topological Dirac semimetal (TDS) KZnBi via AC THz chiral anomaly. The crystal lattice of 3D TDS KZnBi is constructed by alternative stacking of planar ZnBi honeycomb layers and K atoms (*19*), which has the threefold rotational and inversion symmetries that protect 3D Dirac states composed of the Zn-4s and Bi-6p orbitals (Fig. 1A). The simple band structure with only two Dirac cones and an extremely small Fermi surface (FS) (*19*) can take advantage of a clear separation of a Dirac cone to two chiral Weyl cones under a relatively low $\boldsymbol{B}$ (Fig. 1B, left). Furthermore, when two chiral Weyl cones form under the applied $\boldsymbol{B}$, applying additional THz electric field, $\boldsymbol{E}_{THz}$, induces the THz charge pumping (CP) between two chiral states, leading to a nonzero current flow, $\boldsymbol{J}_{chiral}$, of the CFs via an intervalley relaxation (R_{inter}) as indicated by a red arrow (Fig. 1B, right) (*20*) while remaining the CFs under intravalley scatterings (S_{intra}) at the Fermi level (E_F). Thus, two types of plasmas, namely, R_{inter} plasma and S_{intra} plasma, at E_F coexist during the THz CP process.

In the near-field THz spectroscopy (Fig. 1C), as the pulsed $\boldsymbol{E}_{THz}$ efficiently generates the chiral anomaly induced current flow, the THz near-field probe enables exclusive detection of the real-space $\boldsymbol{J}_{chiral}$ distribution. First, the pulsed transient $\boldsymbol{E}_{THz}$ has a strong field intensity [approximately 100 times greater than the continuous $\boldsymbol{E}_{DC}$ used in transport measurements in (*19*, *21*)], generating a high-density $\boldsymbol{J}_{chiral}$. This provides a clear difference in the transmitted $\boldsymbol{E}_{THz}$ even under weak $\boldsymbol{B}$ of 0.23 T (Fig. 1C, inset graph). Second, the transmitted $\boldsymbol{E}_{THz}$ can classify the R_{inter} and S_{intra} based on their different plasma frequency (ω_p) and scattering rate (γ) (*22*, *23*). The characterized plasma of CFs is not the bulk plasmon, a longitudinal electron oscillation, which cannot directly couple to the transverse $\boldsymbol{E}_{THz}$. Moreover,

[1]Department of Energy Science, Sungkyunkwan University, Suwon 16419, Republic of Korea. [2]Center for Integrated Nanostructure Physics, Institute for Basic Science, Sungkyunkwan University, Suwon 16419, Republic of Korea. [3]Department of Physics, Yonsei University, Seoul 03722, Republic of Korea. [4]Department of Physics, Korea Advanced Institute of Science and Technology, Daejeon 34141, Republic of Korea. [5]Department of Physics, University of Ulsan, Ulsan 44610, Republic of Korea.
*Corresponding author. Email: kimsungwng@skku.edu
†These authors contributed equally to this work.

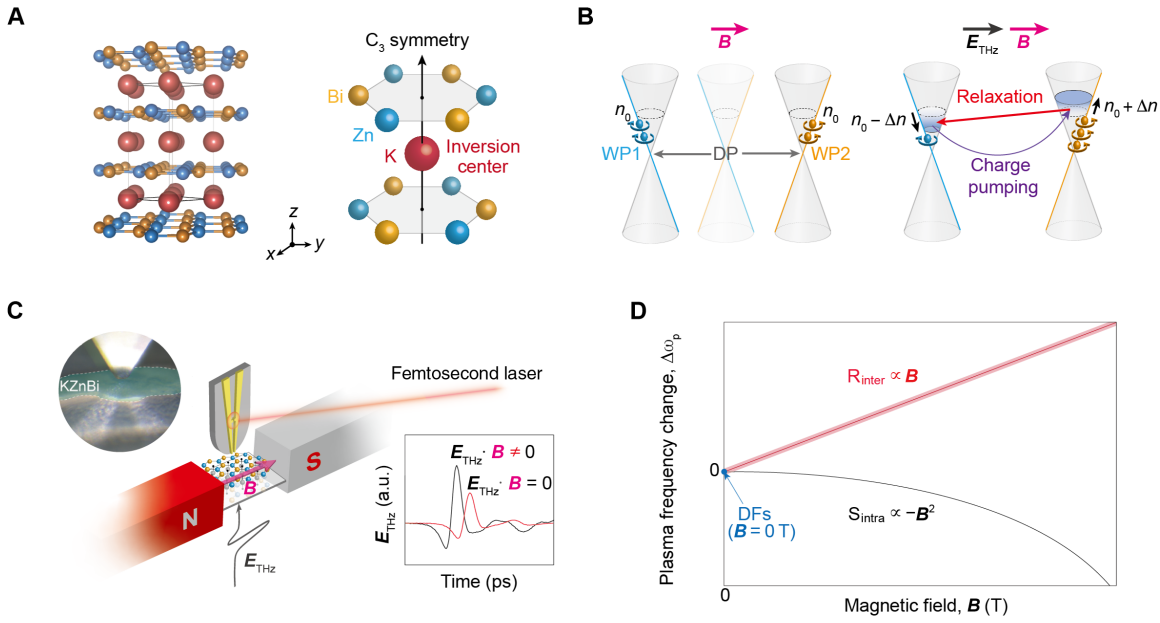

Fig. 1. Strategy for measuring the electrodynamics of the R_{inter} in a 3D TDS KZnBi. (**A**) Crystal structure of KZnBi (left). Color balls represent K (red), Zn (sky blue), and Bi (yellow) atoms. Unit cell is indicated by black solid lines. Black arrow indicates a C_3 rotational symmetry, and K atom is the center of the inversion symmetry (right). (**B**) Chiral anomaly induced by collinear $\boldsymbol{E}_{THz}$ and $\boldsymbol{B}$ in a 3D TDS KZnBi. Under $\boldsymbol{B}$, the Dirac cone (DP) splits into two Weyl cones (WP1 and WP2) with balanced charge density n_0. The charge imbalance ($2\Delta n$) is induced by a chiral CP (purple arrow), which gives $\boldsymbol{J}_{chiral}$ during a relaxation (red arrow) by applying $\boldsymbol{E}_{THz}$ field in the same direction to $\boldsymbol{B}$. (**C**) Schematic illustration of near-field magneto-THz spectroscopy. Transmitted THz wave (gray pulse, $\boldsymbol{E}_{THz}$) through the sample (green color in charge-coupled device image, top left) is measured by tip-probe antenna, while the external $\boldsymbol{B}$ is applied by Nd permanent magnets. The $\boldsymbol{E}_{THz}$ signals under $\boldsymbol{E}_{THz} \cdot \boldsymbol{B} \neq 0$ (red line) and $\boldsymbol{E}_{THz} \cdot \boldsymbol{B} = 0$ (black line) are displayed in the inset (bottom right). a.u., arbitrary unit. (**D**) Proposed $\boldsymbol{B}$ dependence of the plasma frequencies of both fermions. The R_{inter} (red line), S_{intra}, and DFs (black line) show the relations of $\omega_p \propto \boldsymbol{B}$ and $\omega_p \propto -\boldsymbol{B}^2$, respectively.

on the basis of the $\boldsymbol{B}$ dependence of ω_p, the THz electrodynamics of $\boldsymbol{J}_{chiral}$ of R_{inter} can be distinguished from the normal current, $\boldsymbol{J}_{normal}$ of S_{intra}. Figure 1D depicts the relation between ω_p and $\boldsymbol{B}$ relation for both R_{inter} and S_{intra} that are derived from combining Boltzmann transport (*4*, *5*) and Drude models (see Methods) (*22*–*25*). It is noted that the unknown relation of ω_p and $\boldsymbol{B}$ for the S_{intra} is first revealed from our experiments. The $\boldsymbol{J}_{chiral}$ and $\boldsymbol{J}_{normal}$ are visualized in real space by near-field spectroscopy (*23*, *26*, *27*). The primary capability of the near-field method is that the local Drude conductance σ satisfying $\boldsymbol{J} = \sigma \boldsymbol{E}_{THz}$ can be imaged by scanning the tip-probe detector (*23*, *26*, *27*). This RT accessibility of THz near-field spectroscopy to each CF with distinct electrodynamic parameters overwhelms low-temperature magneto-transport measurements having an ambiguity in defining the intrinsic dynamics of the R_{inter} due to the coexisting S_{intra} (*3*–*10*).

First, without $\boldsymbol{B}$, we observe the low-energy electrodynamics of the Dirac fermions (DFs) in KZnBi, such as ultrahigh mobility at RT. Figure 2A shows a THz conductivity (σ_{THz}) with a resolution of ~0.01 THz, presenting the spectral contributions of the DFs and infrared (IR) active phonons by fitting to Drude-Lorentz model (see fig. S1 and Methods for fitting details). For several single crystals, we extract the following THz electrodynamic parameters of the DFs (Fig. 2, B and C): a DC conductivity (σ_{DC}) of ~800 ohms^{-1} cm^{-1}, a plasma frequency (ω_p) of ~45 THz, a scattering rate (γ) of ~1 THz, and a mobility (μ) of ~13,000 cm^2 V^{-1} s^{-1} at RT (see table S1 for all measured samples). For the calculation of μ value, the effective mass of the DFs obtained from transport measurements is used (*19*, *21*). Our findings on the small ω_p and low γ values show a characteristic feature of the DFs with a very high μ (*24*, *25*).

Moreover, we find all-optical evidence for the 3D Dirac semimetallic band of KZnBi from the characteristic singularity and interband transition in the IR spectrum (Fig. 2, D to F). The IR conductivity (σ_{IR}) in Fig. 2D shows both the strong absorption peak and linear absorption feature, originating from van Hove singularity (ΔE_{vHs}) and optical interband transition (ΔE_{inter}) within the Dirac band, respectively (see fig. S2 for fitting details) (*28*, *29*). Combined with the 3D Dirac model (*28*), we extract the Fermi velocity (v_F) of ~0.85×10^5 m/s and E_F of ~96 meV below the Dirac points, consistent with the obtained values in transport measurements (*19*, *21*). All samples show similar v_F and E_F values (Fig. 2E and table S2). By integrating the physical properties obtained from the IR ellipsometry, we construct a band structure of KZnBi (Fig. 2F), whose 3D Dirac band is consistent with density functional theory (DFT) calculation and angle-resolved photoemission spectroscopy data (*19*).

We confirm chiral anomaly at RT from the σ_{THz} spectrum under in-plane $\boldsymbol{B} \parallel \boldsymbol{E}_{THz}$ ($0\ T \leq \boldsymbol{B} \leq 0.23\ T$), where two Drude responses of the R_{inter} and S_{intra} evolve in a complementary manner. As shown in Fig. 3A, a single Drude peak of the DFs at $\boldsymbol{B} = 0$ T is observed, whereas an additional sharp Drude feature that appears as $\boldsymbol{B}$ is increased. Here, the sharpness of the new Drude peak can be explained by the suppressed intervalley scatterings between two Weyl cones of opposite chiralities, resulting from a $\boldsymbol{B}$-induced axial splitting of the 3D Dirac cone (*20*, *30*). We also find that the γ (≈ 85 cm^{-1}) values for the DFs and S_{intra} are very close to each other, indicating a minor contribution of chirality in the intravalley scatterings. The

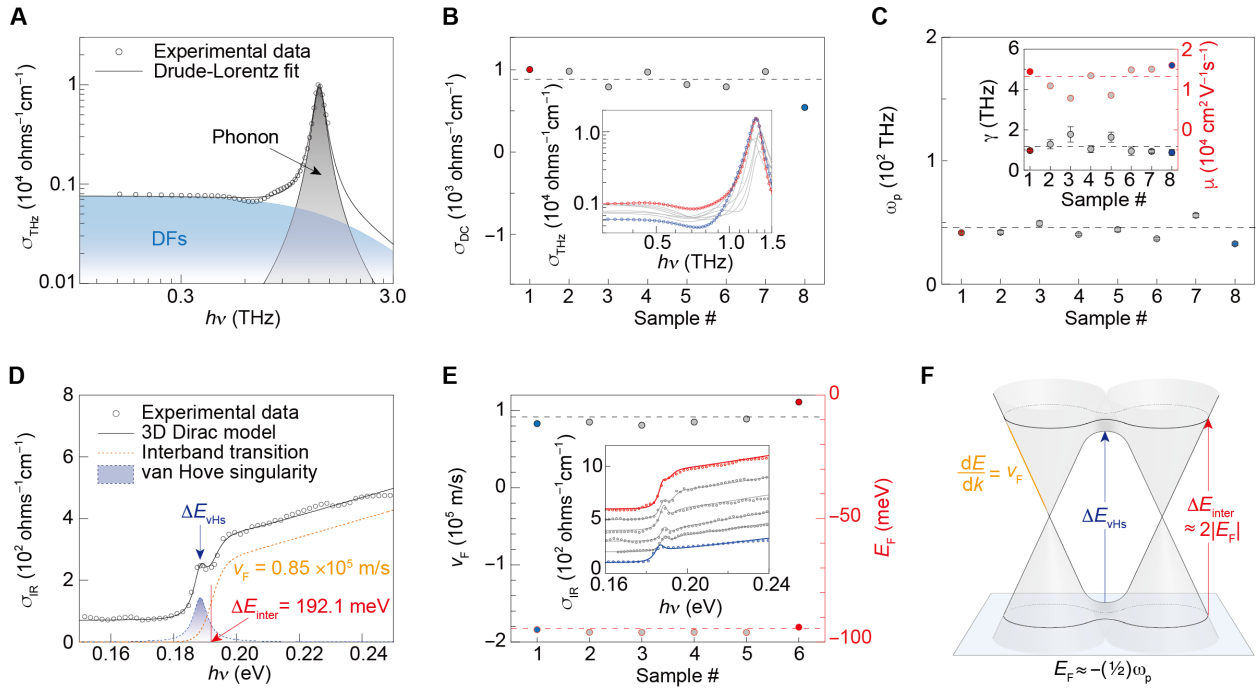

Fig. 2. All-optical identification on 3D TDS state of KZnBi. (**A**) σ_{THz} spectrum and its Drude-Lorentz model analysis. Contributions from the DFs and IR phonon are represented by blue and gray regions, respectively. (**B**) σ_{DC} of several KZnBi samples extracted from raw σ_{THz} spectra (inset). Red and blue dots are the highest and lowest σ_{DC} values, respectively. The dashed line is an averaged value. (**C**) ω_p (main panel), γ (left axis of the inset), and μ (right axis of the inset) of the nonchiral DFs. Dashed lines are averaged values of each parameter. (**D**) σ_{IR} spectrum and its 3D Dirac model analysis, giving a van Hove singularity (navy region indicated by a blue arrow, ΔE_{vHs}), interband transition (indicated by red line and arrow, ΔE_{inter}), and v_F (orange dashed line). (**E**) v_F and E_F values extracted from σ_{IR} spectra (inset) for several samples. The black and red dashed lines are their averaged values. Red and blue dots are the highest and lowest v_F values, respectively. (**F**) Band structure of 3D TDS KZnBi constructed based on the analysis of the σ_{THz} and σ_{IR} data. The relationship of $E_F \approx -(1/2)\omega_p$ is found.

ω_p values further provide the carrier density of ~8.3×10^{17}/cm^3 for the DFs and that for the S_{intra} ranging from ~6.85×10^{16}/cm^3 ($\boldsymbol{B}$ = 0.06 T) to ~7.02×10^{15}/cm^3 ($\boldsymbol{B}$ = 0.23 T) (see fig. S3). The gradual increase of the sharp Drude peak of R_{inter} is accompanied by a monotonic decrease of the broad Drude peak of S_{intra}, signaling the chiral CP (*3*–*10*). Therefore, it is shown that KZnBi can host distinguished chiral CP between Weyl cones, where the chemical potential imbalance is determined by the CP rate of $\boldsymbol{E}_{THz} \cdot \boldsymbol{B}$. This THz chiral anomaly was also presented in the far-field measurements of another 3D TDS Cd_3As_2 (*20*). A similar RT chiral anomaly has also been suggested in Cd_3As_2 through nonlocal transport measurements (*17*). This robustness can be ascribed as a role of topological protection, guaranteeing the possibility of RT dissipationless $\boldsymbol{J}_{chiral}$ (*31*–*33*). It is notable that, in our experiments, a chiral anomaly occurs at a very weak $\boldsymbol{B}$. This unexpected result can be explained by the extremely small FS (*21*) and substantial $\boldsymbol{B}$-induced band splitting due to a large *g*-factor arising from the spin-orbit coupling and layered structure of KZnBi. The band splitting can be estimated from the saturation of anomalous Hall resistance, giving the Weyl points split by ~0.02 Å^{-1} when $\boldsymbol{B} \approx 0.25$ T (*21*). This $\boldsymbol{B}$-induced splitting size is comparable to that of the inversion symmetry broken Weyl semimetals (*34*–*36*). In addition, the IR-active phonons at 1.4 THz become suppressed with the decrease of spectral weight (= area under phonon peak) and the shift to lower frequencies (Methods).

To unambiguously elucidate the intrinsic electrodynamics of $\boldsymbol{J}_{chiral}$, we use two-fluid Drude (*20*, *25*) and generalized Lorentz (*37*) models, which enables us to exclude the other contributions from the DFs, S_{intra}, and phonon (Fig. 3B and fig. S3). A significant difference in their γ values of 1/3 THz and 1 THz is used to separate Drude responses of the R_{inter} and S_{intra} from the total σ_{THz} spectra, respectively (fig. S3 and Methods). The spectral weights (= area underneath the Drude peak) of major S_{intra} (blue region in the left panel) and minor R_{inter} at 0.06 T changes to those of major R_{inter} (red region in the right panel) and minor S_{intra} at 0.20 T. It is remarkable that the complete transition is accomplished under weak $\boldsymbol{B}$ of 0.23 T, where the dominance of R_{inter} for $\boldsymbol{J}_{chiral}$ reaches more than 99.3% (see fig. S3 for the systematic $\boldsymbol{B}$-dependent transition). $\boldsymbol{B}$ of 0.23 T for the dominant generation of $\boldsymbol{J}_{chiral}$ in the present RT THz spectroscopy is significantly low compared to that (a few tesla) for inducing the chiral anomaly in cryogenic transport measurements (*3*–*10*). In this study, such practical accessibility to $\boldsymbol{J}_{chiral}$ was made by a combination of THz spectroscopy providing a strong $\boldsymbol{E}_{THz}$, with 3D TDS KZnBi showing a significant Weyl cone splitting in weak $\boldsymbol{B}$.

The separated σ_{THz} encompasses the distinct electrodynamics of both the R_{inter} and S_{intra}. Tracking the THz parameters as a function of $\boldsymbol{B}$ leads to the hallmark for each fermion (Fig. 3, C and D). Primarily, ω_p shows an unprecedented linear relation to $\boldsymbol{B}$ for the R_{inter} (Fig. 3C), and the result matches well with the theoretical model (Fig. 1D and Methods). As similar results have been reported for Cd_3As_2 (*20*) [although the required $\boldsymbol{B}$ is an order of magnitude smaller for KZnBi, probably due to the contrasting sizes of both *g*-factor and FS, estimated from the Shubnikov–de Haas oscillation (*21*, *38*)], we consider that this linear relationship is a common property of TDSs. Furthermore, the relation that ω_p of the S_{intra} is

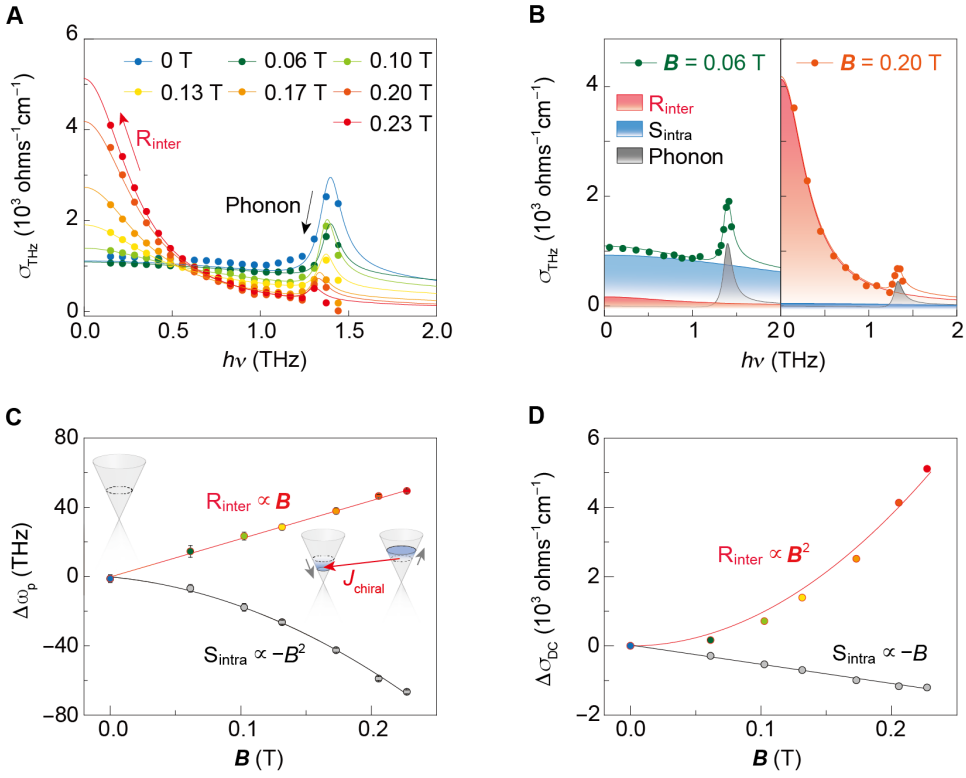

Fig. 3. Electrodynamic control principle of the CFs in KZnBi. (**A**) σ_{THz} (circles) spectra under various $\boldsymbol{B}$ and their model fitting results (lines). Red and black arrows indicate the generation of the R_{inter} and suppression of the phonons, respectively. (**B**) σ_{THz} spectra for $\boldsymbol{B}$ = 0.06 T (green dots and line, left) and 0.20 T (red dots and line, right) contributed from the R_{inter} (red region), S_{intra} (blue region), and phonons (gray region). We note that the total charge is conserved as a sum of R_{inter}, S_{intra}, and anomalous Hall carriers (not shown here). (**C** and **D**) $\boldsymbol{B}$ dependences of $\Delta\omega_p$ (C) and $\Delta\sigma_{DC}$ (D) for R_{inter} and S_{intra}, where the $\Delta\omega_p$ and $\Delta\sigma_{DC}$ indicate the $\boldsymbol{B}$-induced changes in the ω_p and σ_{DC}. Colored (gray) dots for R_{inter} (S_{intra}) are experimental data. Their best fits are represented by red (gray) lines. Insets in (C) illustrate the electronic states for $\boldsymbol{B}$ = 0 T (left) and 0.23 T (right). Red arrow in the right inset indicates $\boldsymbol{J}_{chiral}$.

proportional to $-B^2$ is uncovered. This opposite sign of the ω_p changes reflects that the carriers of J_{chiral} in the intervalley relaxation are immigrated from which were inside the Weyl cones through the CP process, relating to charge conservation in a 3D TDS. We note that the missing spectral weight can be compensated by the cyclotron resonance at higher frequencies. It is also found that γ of the R_{inter} exponentially decreases with increasing $\boldsymbol{B}$ and that γ of the R_{inter} at 0.23 T is one-third of ~1 THz for the S_{intra}, signaling the long-lived quantum coherent state of $\boldsymbol{J}_{chiral}$ between Weyl cones with an increased distance in momentum space (see fig. S4 for the $\boldsymbol{B}$-dependent γ of the R_{inter}). In addition, another representative parameter σ_{DC} exhibits different $\boldsymbol{B}$ dependences for both CFs (Fig. 3D) as the ω_p. The measured σ_{DC} of the R_{inter} has an ideal quadratic relationship with $\boldsymbol{B}$, showing good agreement with theoretical predictions (*4*, *5*) and another experimental result on THz chiral anomaly in Cd_3As_2 (*20*). Because the emergence of chiral anomaly subtly depends on E_F (*19*, *21*), we carefully selected samples exhibiting both the negative magnetoresistance and anomalous Hall effect within 0 T < $\boldsymbol{B}$ < 0.5 T. By separating the conductance of the R_{inter}, the σ_{DC} of the S_{intra} is revealed to be linearly dependent on $\boldsymbol{B}$. These findings, based on the quantification of electrodynamic parameters, suggest that the control protocol of $\boldsymbol{J}_{chiral}$ is readily available.

We directly map the $\boldsymbol{J}_{chiral}$ flow on the KZnBi single crystal with a large lateral size of ~600 μm by 600 μm by means of a near-field THz probe at RT. The whole sample is uniformly excited by the collinear $\boldsymbol{E}_{THz}$ and external $\boldsymbol{B}$ = 0.10 T. Then, the local $\boldsymbol{E}_{THz}$ within a pixel of 20 μm × 20 μm is scanned with THz tip probe over the sample, resulting in a spatial mapping image of $\boldsymbol{J}_{chiral}$. For reliability, we calculate the $\boldsymbol{J}_{chiral}$ distribution in another way by multiplying a local σ_{THz} in 20 μm × 20 μm and $\boldsymbol{E}_{THz}$ and compare two mapping results and confirm their good consistency (Methods). We mention that the possibility of the current jetting effect can be ruled out by four conditions in our experiments: the contact-free measurements, the small magnitude of applied $\boldsymbol{B}$, the isotropic in-plane conductivity, and the controllable $\boldsymbol{J}_{chiral}$ direction. The occurrence of $\boldsymbol{J}_{chiral}$, which was also confirmed through spectral analysis of far-field THz measurement data at low T and under strong $\boldsymbol{B}$ (*20*), is phenomenologically consistent with our RT near-field THz results. However, our mapping of $\boldsymbol{J}_{chiral}$ imaging a local flow in the real space is distinct from the far-field result (*20*), providing information on the spatially averaged $\boldsymbol{J}_{chiral}$ only in the frequency domain.

Through the near-field THz mapping, we succeed in visualizing the chiral anomaly in real space. As shown in Fig. 4A, when $\boldsymbol{E}_{THz}$ is collinear to $\boldsymbol{B}$ = 0.10 T (i.e., maximal $\boldsymbol{E}_{THz} \cdot \boldsymbol{B}$), $\boldsymbol{J}_{chiral}$ is found to be nonuniform and is shifted along the field direction. On the other hand, for $\boldsymbol{E}_{THz} \cdot \boldsymbol{B} = 0$, no clear shift of the uniform $\boldsymbol{J}_{normal}$ of S_{intra} is observed (see also fig. S5 where the homogeneous irradiation of $\boldsymbol{E}_{THz}$ to the whole sample area is verified from the uniform distribution of $\boldsymbol{J}_{normal}$ of DFs without chiral CP). The biased $\boldsymbol{J}_{chiral}$ maintained over the pulse duration (~1 ps) reflects a nonequilibrium

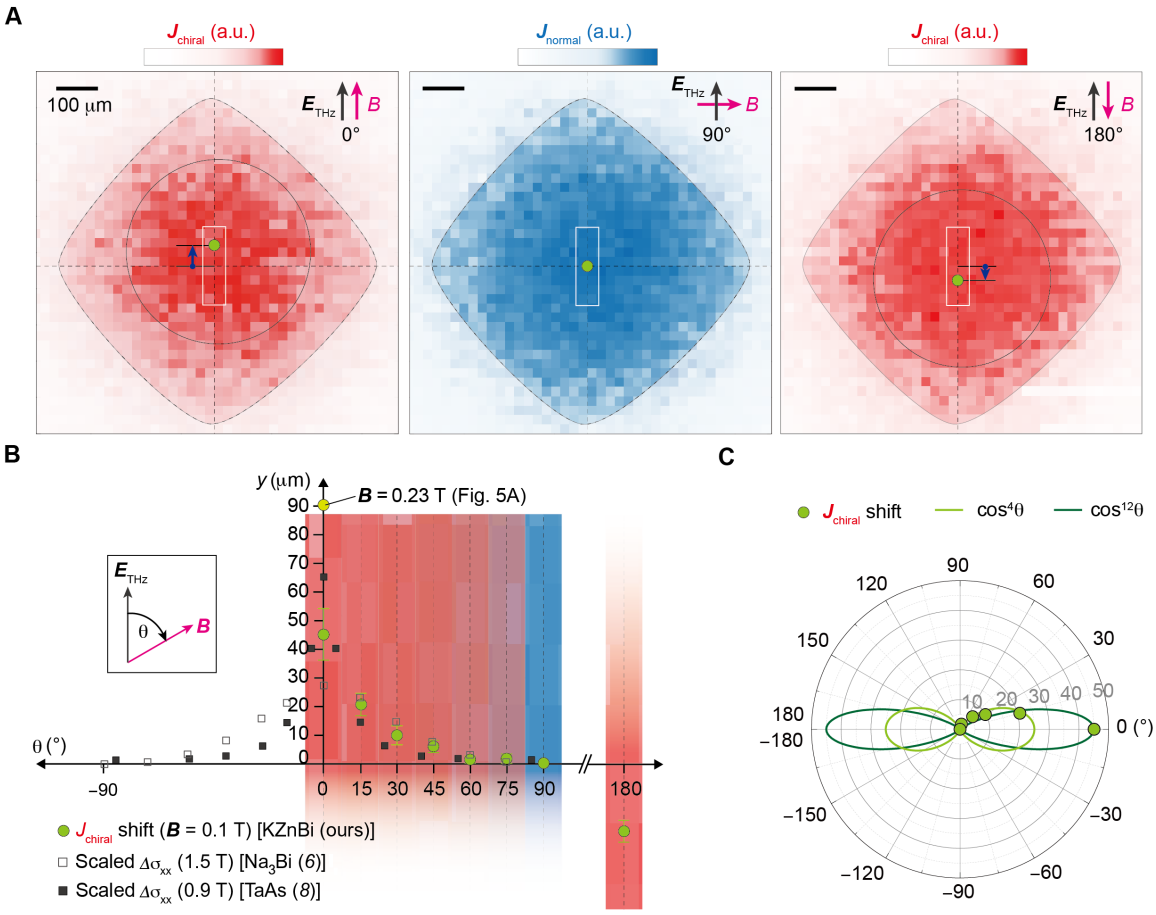

Fig. 4. Visualization of chiral anomaly in real space. (**A**) The current distributions depending on the configuration of $\boldsymbol{E}_{THz}$ and $\boldsymbol{B}$ = 0.10 T. For the left, middle, and right panels, $\boldsymbol{E}_{THz}$ is parallel, perpendicular, and antiparallel to $\boldsymbol{B}$, respectively. The opposite shift (blue arrows) of the localized current is observed for the parallel and antiparallel cases (i.e., maximal $\boldsymbol{E}_{THz} \cdot \boldsymbol{B}$), while the no shift of uniform distribution is measured for the perpendicular case (i.e., $\boldsymbol{E}_{THz} \cdot \boldsymbol{B} = 0$). (**B**) $\boldsymbol{E}_{THz} \cdot \boldsymbol{B}$ dependence of the $\boldsymbol{J}_{chiral}$ shift. The centers (green circles) of $\boldsymbol{J}_{chiral}$ shifts are collected from the rectangular cuts [white lines in (A)] in the current distribution images. The $\boldsymbol{J}_{chiral}$ shift for $\boldsymbol{B}$ = 0.23 T (yellow circle; Fig. 5A) is also plotted. For a direct comparison with 3D Dirac semimetal Na_3Bi (*6*) and Weyl semimetal TaAs (*8*), a relation of $\boldsymbol{J} = \sigma\boldsymbol{E}$ is used. (**C**) Polar plot of the $\boldsymbol{J}_{chiral}$ shift, following $\cos^4\theta$ dependence at large θ and $\cos^{12}\theta$ dependence at small θ.

state of chiral anomaly, which is supported by the chiral anomaly induced Drude peak of τ ~ 3 ps (Fig. 3A). With varying θ = arg($\boldsymbol{E}_{THz} \cdot \boldsymbol{B}$) from 0° to 90°, the amount of $\boldsymbol{J}_{chiral}$ shift radically decreases (Fig. 4B and fig. S6), showing a chiral plume suggested from the angular magneto-conductance in transport experiments (*6*, *8*). Such direct visualization of the chiral plume through the near-field measurements provides insight into the real-space chiral anomaly, complementary to the spectral analysis of conventional far-field THz studies on the chiral anomaly (*20*). The θ-dependent $\boldsymbol{J}_{chiral}$ shift follows a $\cos^4\theta$ function at large θ similar to that for Na_3Bi (*6*) and $\cos^{12}\theta$ dependence at small θ. The sharpness of the chiral plasma plume in KZnBi may be associated with the planar honeycomb lattice with sp^2-hybridized bonding, focusing on chiral CP on the ZnBi plane, distinct from the buckled honeycomb lattice of Na_3Bi with the contribution of sp^3-hybridized bonding character, where the interlayer chiral CP can also be occurred. This angular behavior provides direct evidence that we measure the real-space chiral anomaly and visualize the $\boldsymbol{J}_{chiral}$ distribution at RT.

Last, by varying the direction of $\boldsymbol{E}_{THz}$, we achieve a directional control of pure $\boldsymbol{J}_{chiral}$ distributed on the KZnBi (~600 μm by 800 μm) under external $\boldsymbol{B}$ = 0.23 T (~99.3% of R_{inter} dominance; fig. S3). The main panels of Fig. 5A present the opposite flow of $\boldsymbol{J}_{chiral}$ in the spatial distribution according to the direction of $\boldsymbol{E}_{THz}$. From the field-dependent position of $\boldsymbol{J}_{chiral}$ distribution, one can recognize that $\boldsymbol{J}_{chiral}$ is shifted along the direction of $\boldsymbol{E}_{THz}$. The side panels display spatial distribution curves (SDCs) representing local $\boldsymbol{E}_{THz}$ intensities along both horizontal and vertical lines across the center of the sample. In the vertical direction (parallel to both $\boldsymbol{E}_{THz}$ and $\boldsymbol{B}$), the SDCs exhibit an asymmetric $\boldsymbol{J}_{chiral}$ distribution (side panels), which reflects the flow of $\boldsymbol{J}_{chiral}$ induced by the chiral CP. This is in contrast to the nearly symmetric distribution (top panels) formed along the horizontal direction (perpendicular to both $\boldsymbol{E}_{THz}$ and $\boldsymbol{B}$). To the best of our knowledge, such THz field–controlled $\boldsymbol{J}_{chiral}$ has not been reported yet using diffraction-limited far-field measurements. Moreover, this $\boldsymbol{J}_{chiral}$ mapping stimulates the real-space understanding of the chiral anomaly from the axial plume of the R_{inter}, which so far has been veiled under conventional momentum-space description. Most of all, our results substantiate that the sign of $\boldsymbol{E}_{THz} \cdot \boldsymbol{B}$ determines the direction of the chiral CP between Weyl cones in momentum space and, that is, the direction of nonzero $\boldsymbol{J}_{chiral}$ flow in

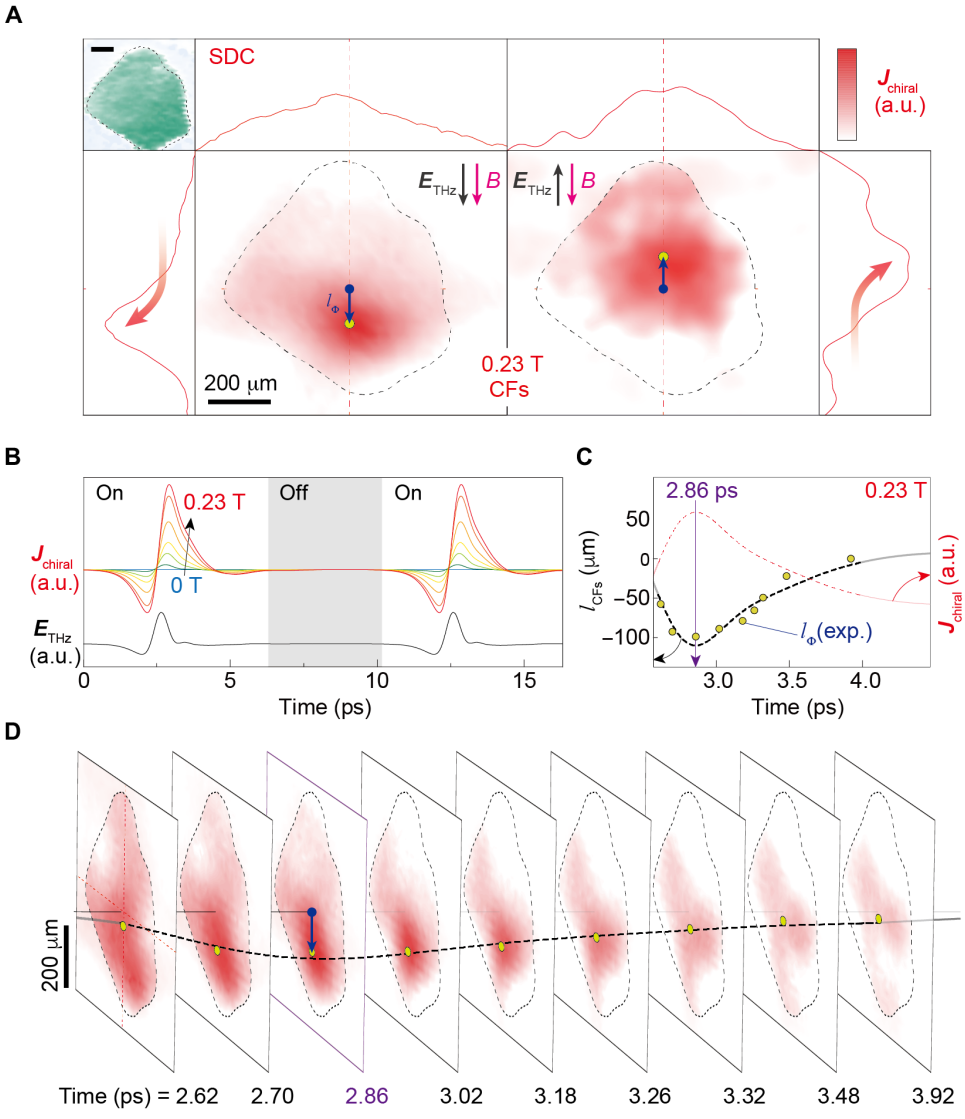

Fig. 5. Control of J_{chiral} in temporal and spatial domains. (**A**) The J_{chiral} mapping images (main panel) obtained under 0.23 T for each pulsed E_{THz}. In the top left, the dashed line indicates the sample area (green region). Scale bar, 200 μm. The intensity of J_{chiral} is represented by the darkness of red color. Red dashed lines represent the center of the sample. Dark blue and yellow circles are the maxima of J_{chiral} distributions before and after applying E_{THz} and B, respectively. Spatial distribution curves (SDCs) of the J_{chiral} intensity are shown in top, leftmost, and rightmost panels. Red thick curved arrows indicate the change of intensity, i.e., the J_{chiral} flow. (**B**) Temporal J_{chiral} intensity (top) under $0\ T \leq B \leq 0.23\ T$ acquired from a convolution of incident E_{THz} pulse (bottom) and experimental σ_{THz} of the R_{inter}. (**C**) The experimental J_{chiral} intensity (red dashed line) and calculated l_{CFs} (black dashed line). A maximal shift of J_{chiral} appears at 2.86 ps (purple arrow). The l_Φ values [yellow dots extracted from the J_{chiral} mapping images in (D)] are superimposed on the l_{CFs} curve. (**D**) Time-resolved J_{chiral} mapping images, where snapshots at $2.62\ ps \leq t \leq 3.92\ ps$ show the dynamics of the J_{chiral} distribution in real space with time-dependent shifts [yellow circles in (C) and (D)] connected by a black dashed line for clarity. The time resolution of E_{THz} is 0.08 ps.

real space. The opposite direction of J_{chiral} flow in Fig. 5A is thus a definite evidence that the real-space J_{chiral} flow is manipulated by the chiral CP direction.

Unexpectedly, at RT, the macroscopic J_{chiral} distribution shows a coherent flow more than ~100 μm in ~1 ps, on average. The chiral CP induces the shift of the maximum J_{chiral} position without destroying its shape. The phase distribution of transmitted E_{THz} shows a nearly identical value at the central region of the J_{chiral} image, supporting the phase coherence of the J_{chiral} flow in KZnBi (see fig. S7). We emphasize that the coherence transport length (l_Φ) is comparable to or even greater than the mean free path of the R_{inter} ($\langle l_{CFs} \rangle$ ~ 50 μm) at RT, exceeding the ballistic transport length of ~10 μm at 5 K of photocurrent in the topological semimetal $ZrTe_5$ (*31*). In addition, the present J_{chiral} evolution induced by time-reversal symmetry breaking is distinct from the case of Weyl semimetals where a crystal symmetry breaking induces the J_{chiral} (*18*, *31*, *33*, *39*), providing a further opportunity to study chiral anomaly induced real-space phenomena in various Dirac semimetals. On the other hand, the J_{normal} exhibits a negligible shift in the THz current mapping image in contrast to the J_{chiral} having a giant net flow (see figs. S5 and S6). The unique accessibility to the real-space J_{chiral} of the near-field probe unveils another intrinsic property of chiral anomaly, i.e., the macroscopic coherence length.

Beyond the spatial visualization, we further estimate the temporal dynamics of J_{chiral} and its B-dependent evolution, both of which

are strongly correlated with σ_{THz} and $\boldsymbol{E}_{THz}$. The $\boldsymbol{J}_{chiral}$ (t) curves (Fig. 5B) are calculated by resorting to a convolution between the σ_{THz} of R_{inter} at a given $\boldsymbol{B}$ and incident $\boldsymbol{E}_{THz}$. For all $\boldsymbol{B}$, the resulting $\boldsymbol{J}_{chiral}$ ($\boldsymbol{B}$) are immediately generated after the $\boldsymbol{E}_{THz}$ is incident to the KZnBi sample. As $\boldsymbol{B}$ is increased, both the intensity and the duration of $\boldsymbol{J}_{chiral}$ are increased. At $\boldsymbol{B}$ = 0.23 T, $\boldsymbol{J}_{chiral}$ is lastly prolonged more than ~3 ps, which is corresponding to the momentum relaxation time of the chiral anomaly induced R_{inter} ($\tau \sim 3$ ps from $\gamma \sim {}^1/_3$ THz; see fig. S4). Moreover, the calculated $\boldsymbol{J}_{chiral}$ gives the length scale of the $\boldsymbol{J}_{chiral}$ as shown in Fig. 5C, which implies that the time-dependent l_{CFs} is longer as the $\boldsymbol{J}_{chiral}$ intensity becomes stronger. Therefore, tracking the picosecond dynamics could be of benefit to materializing and controlling $\boldsymbol{J}_{chiral}$ in spacetime.

All the above electrodynamics are integrated into imaging the $\boldsymbol{J}_{chiral}$ in both temporal and spatial domains by the time-resolved mapping of spatial $\boldsymbol{J}_{chiral}$ distribution (Fig. 5D). Continuous snapshots of the $\boldsymbol{J}_{chiral}$ distributions in 2.62 ps ≤ time (t) ≤ 3.92 ps with a time resolution of 0.08 ps (fig. S8) show the change in the transport length of axial plumes from 15 μm (t = 2.62 ps) to ~100 μm (t = 2.86 ps) to 5 μm (t = 3.92 ps), demonstrating the dynamics of $\boldsymbol{J}_{chiral}$ distribution in real space for a pulse duration (~1 ps). A connecting line of $\boldsymbol{J}_{chiral}$ maxima in the spatial domain at each snapshot is identical to the calculated l_{CFs} curve (Fig. 5C) in the temporal domain, providing compelling evidence for the establishment of a real-space electrodynamic model for the CFs with chirality. Our protocol for measuring and controlling the topological $\boldsymbol{J}_{chiral}$ of long-lived coherence under weak $\boldsymbol{B}$ at RT will innovate high-fidelity information devices and pave a practical route toward chiraltronics.

METHODS

Preparation of KZnBi sample for magneto-THz experiments

The KZnBi single crystals with an emerald color, shiny, and planar surface were synthesized via the self-flux method with the excess of K metal, and their crystal structures with planar honeycomb layers (Fig. 1A) were identified from XRD θ-2θ pattern and φ scan in our previous work (*19*). By repeating the cleaving, layered KZnBi crystals became thinner, down to the thickness of ~10 μm, where the samples were transparent in the THz spectral region. The thickness was measured from the time of flight of femtosecond laser photon reflected from the top surface of the sample. The uniformity of the samples was confirmed by the nearly consistent time delays of the transmitted E_{THz} over the sample. The cleaved KZnBi crystals were transferred onto the Al_2O_3 sapphire (0001) substrate that shows no prominent spectral feature in the THz region. The crystals were covered by polymer tape or a cover glass as capping layers with a negligible THz response, which do not hamper the spectral analysis. The cleaving, transferring, and covering processes were conducted in the glove box to protect from degradation, such as aging and oxidation. For near-field magneto-THz spectroscopy, all the samples were carefully checked to be suitable for a routine use through a trial-and-error procedure.

Derivation of ω_p versus B for CFs

The light-matter interaction provides the spectroscopic evidence for the chiral anomaly through a distinct plasma oscillation. The THz experiment provides the σ_{THz} spectra, whose underneath area corresponds to the ω_p (proportional to the n). The measured σ_{THz} can be interpreted with AC Drude model written as

$$\sigma THz = \omega_p^2 \tau / [4\pi(1 - i\omega\tau)] \quad (1)$$

where τ is relaxation time. Together with the conductivity for chiral anomaly derived from Boltzmann transport theory, we find a relationship between the ω_p and $\boldsymbol{B}$ for the R_{inter}

$$\omega_p^2 = (e^2/4\pi^2\hbar c)(v/c)[(e\boldsymbol{B}v)^2/E_F^2] \quad (2)$$

where e is the elementary charge, ħ is the reduced Planck constant, v_F is the Fermi velocity, and c is the light velocity in vacuum. We highlight that the ω_p linearly increases with the $\boldsymbol{B}$, deriving a uniqueness for the plasma of R_{inter}. We also note that, through the relation $\omega_p^2 = \sigma_{DC}\tau/4\pi$, the ω_p is related with the DC conductivity (σ_{DC}) and relaxation time (τ). This implies that the ω_p exhibits a characteristic value for each type of charge carriers, allowing the separable detection of the chiral Dirac plasma from the nonchiral one. Hence, the detection of the ω_p as a function of $\boldsymbol{B}$ should be crucial for identifying the chiral anomaly through magneto-THz spectroscopy.

Experimental setting for controlling $\boldsymbol{J}_{chiral}$ in our near-field THz spectroscopy

Near-field magneto-THz spectrometer (Protemics GmbH, TeraCube Scientific) was used to investigate low-energy electrodynamics of 3D TDS KZnBi single crystal. The femtosecond pulse from Ti:sapphire laser (with a center wavelength of 780 nm, a repetition rate of 80 MHz, and an average power of 4 mW) was divided by a beam splitter to generate and detect the $\boldsymbol{E}_{THz}$. For the THz generation, the femtosecond pump pulse was illuminated onto a THz photoconductive antenna as the conventional. In addition, the femtosecond probe pulse was injected onto the THz tip-probe antenna (TeraSpike TD-800-X-HR-WT), which is a 2-μm gap Au electrode patterned on a 1-μm-thick GaAs substrate grown at low temperature. The tip-based THz detection enables the measurement of tiny samples with a lateral dimension of a few micrometers, overcoming a diffraction limit of a typical far-field THz spectroscopy (fig. S5A). The $\boldsymbol{E}_{THz}$ pulse probed in a time domain was transformed into the THz spectrum through fast Fourier transformation. The resulting spectrum ensures a reliable bandwidth of 0.1 to 2.0 THz with a significant signal-to-noise ratio of more than 100, at least, validating our spectral analysis for the DFs, S_{intra}, R_{inter}, and phonon (Figs. 2A and 3, A and B). To generate the R_{inter} in the KZnBi by the CP, the $\boldsymbol{B}$ of 0 to 0.23 T was applied along the honeycomb layer using Nd magnets, together with the parallel $\boldsymbol{E}_{THz}$. Although all the measurements were carried out at RT, the spectral changes of the R_{inter} and phonon with varying the $\boldsymbol{B}$ were observed (Fig. 3, A and B), signaling the robustness of the R_{inter} due to topology. The coincidence between the data measured with a time interval proves the endurance of the sample for 3 days, on average, without degradations in our experimental environments, substantiating the stability of our THz mapping data that is acquired in a day or shorter (depending on the setting of a spatial resolution). Most of all, near-field magneto-THz spectroscopy allows the mapping of the electrodynamic parameters such as conductance, leading to the observation of $\boldsymbol{J}_{chiral}$ distribution (Figs. 4 and 5).

THz conductivity analysis for determining CFs with phenomenological model

From experiments, the $\boldsymbol{E}_{THz}$ signals transmitted through the reference (sapphire substrate) and sample (KZnBi single crystal on the substrate) were measured, presenting a relative shift and a peak reduction

in a time domain. Through Fourier transformation of the $\boldsymbol{E}_{THz}$, the transmittance $\hat{t} = \sqrt{T} \cdot \exp(i\varphi)$ was obtained. On the basis of Tinkham's formula (*22*, *25*), the experimental σ_{THz} was obtained from the ratio of $\hat{t}_{f+s}$ for the sample (KZnBi + substrate) to $\hat{t}_s$ for the substrate with the thin-film and long-wavelength approximations. Note that the exact calculations with Fresnel equation (*22*) were conducted additionally to judge the appropriateness of the approximations.

The σ_{THz} analyses were performed to find and understand the characteristic spectrum of DFs, R_{inter}, S_{intra}, and phonons as below (see Fig. 2A and fig. S3 for fitting results):

(i) [$\boldsymbol{B}$ = 0 T] Drude-Lorentz model for the DFs and phonons

$$\sigma(\omega) = i\omega^2_{p,DFS}/[4\pi(\omega + i\gamma_{DFs})] + \omega\Omega^2_p/[4\pi i(\Omega^2_0 - \omega^2 - i\Gamma_p\omega)] \quad (3)$$

where $\omega_{p,DFs}$ is the plasma frequency of DFs, γ_{DFs} is the scattering rate of DFs, Ω_p is the oscillator strength of phonon, Ω_0 is the center frequency of phonon, and Γ_p is the linewidth of phonon. The model analysis allows determining the electrodynamic parameters of the DFs and phonons (table S1 and fig. S1) without $\boldsymbol{B}$, ensuring the identification of those of the R_{inter} generated under $\boldsymbol{B}$.

(ii) [0 T < $\boldsymbol{B} \leq$ 0.23 T] Two Drude–(generalized) Lorentz model (*37*) for the generated R_{inter} and coupled phonons by the chiral CP

$$\sigma(\omega) = i\omega^2_{p,CF1}/[4\pi(\omega + i\gamma_{CF1})] + i\omega^2_{p,CF2}/[4\pi(\omega + i\gamma_{CF2})] + \omega\Omega^2_p(q - i)^2/[4\pi i(\Omega^2_0 - \omega^2 - i\Gamma_p\omega)|q^2 - 1|] \quad (4)$$

where $\omega_{p,CF1(2)}$ is the plasma frequency of R_{inter} (S_{intra}), $\gamma_{CF1(2)}$ is the scattering rate of R_{inter} (S_{intra}), and q is the Fano asymmetry parameter of phonon. In addition to the ω_p (B) of R_{inter} that shows consistency to our derivation result (see main text and the "Derivation of ω_p versus $\boldsymbol{B}$ for CFs" section), the obtained τ ($\boldsymbol{B}$) values are well explained with theory (*4*, *5*), in which the R_{inter} has a momentum relaxation time longer than the S_{intra} due to the valley separation under $\boldsymbol{B}$ (see fig. S4). From the model analysis, the electrodynamic parameters of R_{inter} were quantified, and the phonon parameters were determined as clear evidence for the generation of R_{inter} by the chiral CP.

Acquisition of J_{chiral} mapping image for visualizing the chirality of fermions

On the basis of our derivation of the $\Delta\omega_p$ ($\propto \boldsymbol{B}$) for the R_{inter} and theoretical predictions for the $\boldsymbol{J}_{chiral}$ ($\propto \boldsymbol{B}$) (*4*–*6*), a local mapping of the THz $\boldsymbol{J}_{chiral}$ ($\propto \Delta\omega_p$) is an appropriate means to visualize the real-space $\boldsymbol{J}_{chiral}$ on the macroscopic sample. The uniform in-plane $\boldsymbol{B}$ of 0.23 T is applied for our $\boldsymbol{J}_{chiral}$ mapping (fig. S5C), where the $\boldsymbol{J}_{chiral}$ is dominant over the $\boldsymbol{J}_{normal}$ due to the nearly complete conversion (Fig. 3, A and C, and fig. S3). The net flow of $\boldsymbol{J}_{chiral}$ ($\propto \Delta\omega_p$ for the R_{inter}) is formed along the $\boldsymbol{B}$ direction, different from a classical Hall current induced by Lorentz force.

For the $\boldsymbol{J}_{chiral}$ mapping, the uniform $\boldsymbol{E}_{THz}$ pump is shined onto the sample and the $\boldsymbol{E}_{THz}$ signals transmitted through the sample for each pixel are detected with the tip probe (see the "Experimental setting for controlling $\boldsymbol{J}_{chiral}$ in our near-field THz spectroscopy" section). The distribution of $\boldsymbol{E}_{THz}$ on the sample shows a time evolution, as the picosecond $\boldsymbol{E}_{THz}$ pump passes through. The σ_{THz} spectrum was acquired at each pixel on the sample by using the Tinkham's formula (*22*, *25*), which leads to the $\boldsymbol{J}_{chiral}$ mapping image (Fig. 5A) by multiplying with the incident $\boldsymbol{E}_{THz}$. Despite a negligible difference in the pixel-to-pixel thickness on the cleaved KZnBi single crystal, the possibility of the distortion in the $\boldsymbol{J}_{chiral}$ distribution was removed by using a relative time delay between the transmitted $\boldsymbol{E}_{THz}$ through the substrate and the sample, which is directly proportional to the optical length (= refractive index × thickness). Thus, the mapping image visualizes the $\boldsymbol{J}_{chiral}$ distributions in real space, whose net flow as a plasma plume is determined by the direction of $\boldsymbol{E}_{THz}$ and $\boldsymbol{B}$ (Fig. 5A) and its intensity is condensed, showing the intrinsic nature of the $\boldsymbol{J}_{chiral}$. The temporal evolution of the $\boldsymbol{J}_{chiral}$ distribution (Fig. 5D) is measured directly through the mapping of transmitted $\boldsymbol{E}_{THz}$ signals. The snapshots of E_{THz} within 2.62 ps $\leq t \leq$ 3.92 ps were mapped out, showing the dynamics of the $\boldsymbol{J}_{chiral}$ distribution with systematic changes of the maxima positions. The probed $\boldsymbol{E}_{THz}$ images within 2.70 ps $\leq t \leq$ 3.18 ps are particularly similar to the $\boldsymbol{J}_{chiral}$ distribution in Fig. 5A, and all the images are smoothly evolved as the intensity of $\boldsymbol{E}_{THz}$ changes. The inverse fast Fourier transform of the σ_{THz} distribution into a time domain agrees well with the averaged $\boldsymbol{E}_{THz}$ signal, showing the reliability of the time-domain analysis.

Calculation of phonon eigenmode to interpret chirality-lattice coupling

To assign the phonon in our THz spectra, first-principles DFT calculations were performed using the local density approximation, and the projector augmented plane-wave method implemented in the Vienna Ab initio Simulation Package program code. The 3s, 3p, and 4s electrons of K, the 3d and 4s electrons of Zn, and the 6s and 6p electrons of Bi were used as valence electrons. Self-consistency was carried out using a unit cell containing 18 atoms, and an 8 × 8 × 4 k-point mesh was used. The plane-wave basis cutoff energy was set to 600 eV, and the effect of spin-orbit coupling is included. Both atomic position and lattice constants are fully relaxed until the Hellmann-Feynman forces were less than 2×10^{-6} eV Å^{-1}. The phonon frequencies and eigenvectors were determined by the finite displacement method with a $3a \times 3b \times c$ supercell containing 54 atoms implemented in the Phonopy code. The Born effective charge tensors are determined using the density functional perturbation theory to calculate the spectra of IR-active mode. The IR spectrum was calculated using the Phonopy-Spectroscopy package. The linewidths were obtained by computing the third-order force constants and following the many-body perturbative approach implemented in the Phono3py software. On the basis of the results presented in table S3 and fig. S9, the THz phonon is unambiguously attributed to the A_{2u} mode.

The contribution of phonons to the σ_{THz} spectrum also depends on the $\boldsymbol{B}$, giving a systematic change in their electrodynamic characters (fig. S10); the reduced spectral weight (Ω_p) is due to the decreased phonon charge ($\boldsymbol{Q}_{ph}$), red shift of the center frequency (ω_0) implying the decreased spring constant by the electron-phonon coupling (*40*), and the increased asymmetry parameter (1/q, inset) proving the quantum interference between the R_{inter} and phonons (*25*). It is interesting that the ω_p ($\propto$ charges of the R_{inter}, $\boldsymbol{Q}_{chiral}$) has a negative proportional relation with the Ω_p ($\propto$ charges of the phonons, $\boldsymbol{Q}_{ph}$), which evidences the axial electron-phonon coupling (*41*–*43*) between the $\boldsymbol{J}_{chiral}$ and $\boldsymbol{Q}_{ph}$ of the A_{2u} phonon of the KZnBi (fig. S9). This observed relation between electrodynamics of the phonon and R_{inter} provides a way to detect the change in the $\boldsymbol{J}_{chiral}$ from the analysis of the phonon spectrum. In our case, it is difficult to conclude that it is a chiral phonon due to magneto-electricity, like the similar phonon anomaly observed in Cd_3As_2. In particular, almost all suppressed phenomena in weak $\boldsymbol{B}$ are difficult to see as pure phonon

dynamics, so we additionally prove the correlation with the spectral weight of the R_{inter} and assume a situation in which the dipole moment of IR-active phonon is screened out by the R_{inter} (fig. S9). In addition, this axial electron-phonon coupling was initially predicted and observed for a chiral crystal (*41*, *42*), but then it was extended to a situation where the symmetry was broken under the $\boldsymbol{B}$ (*43*), and our results can be considered to correspond to the latter.

To understand the origin of electron-phonon coupling, which is evident from the spectral change of phonon (Fig. 3A and fig. S10A), the direction of atomic vibration and associated phonon charge is found to be crucial. In the A_{2u} mode, Zn and Bi atoms on the honeycomb lattice displace along a vertical direction (//$\boldsymbol{z}$) in an antiparallel manner (fig. S9B). The motions of those atoms result in the phonon effective charge vector ($\boldsymbol{Q}_{ph}$), which can be decomposed into in-plane $\boldsymbol{Q}_{xy}$ and out-of-plane $\boldsymbol{Q}_z$. The $\boldsymbol{Q}_{xy}$ directly couples to $\boldsymbol{E}_{THz}$ // $\boldsymbol{x}$, giving the absorption peak when $\boldsymbol{B}$ = 0 T (Fig. 3A). On the other hand, the $\boldsymbol{Q}_z$ vector induces the $\boldsymbol{J}_{chiral}$ through the axial electron-phonon coupling, which reduces the $\boldsymbol{Q}_0$ by $-\delta\boldsymbol{Q}_{ph}$ (// $\boldsymbol{B}$ and // $\boldsymbol{J}_{chiral}$). Theoretical studies (*41*–*43*) explained such phonon change with the difference in v_F between Weyl cones induced by $\boldsymbol{B}$. The scheme for the chirality-lattice coupling on the ZnBi honeycomb is constructed with the $\delta\boldsymbol{Q}_{ph}$ and $\boldsymbol{J}_{chiral}$ (inset of fig. S10). The observed phonon evolution, which relies on a density of the R_{inter} induced by the chiral CP, is well explained with the real-space scheme of chirality-lattice coupling. To the best of our knowledge, the phonon renormalization (Fig. 3A and fig. S10A) has not been reported yet for the IR-active phonon (with the net $\boldsymbol{Q}_{ph}$), whereas a study on the transformation from Raman-active (with no $\boldsymbol{Q}_{ph}$) to IR-active phonon with the chiral CP was published (*42*).

SUPPLEMENTARY MATERIALS

Supplementary material for this article is available at https://science.org/doi/10.1126/sciadv.abq2479

REFERENCES AND NOTES

1. M. Z. Hasan, C. L. Kane, Colloquium: Topological insulators. *Rev. Mod. Phys.* **82**, 3045–3067 (2010).
2. X. L. Qi, S. C. Zhang, Topological insulators and superconductors. *Rev. Mod. Phys.* **83**, 1057–1110 (2011).
3. N. P. Armitage, E. J. Mele, A. Vishwanath, Weyl and Dirac semimetals in three-dimensional solids. *Rev. Mod. Phys.* **90**, 015001 (2018).
4. D. T. Son, B. Z. Spivak, Chiral anomaly and classical negative magnetoresistance of Weyl metals. *Phys. Rev. B* **88**, 104412 (2013).
5. A. A. Burkov, Chiral anomaly and diffusive magnetotransport in Weyl metals. *Phys. Rev. Lett.* **113**, 247203 (2014).
6. J. Xiong, S. K. Kushwaha, T. Liang, J. W. Krizan, M. Hirschberger, W. Wang, R. J. Cava, N. P. Ong, Evidence for the chiral anomaly in the Dirac semimetal Na_3Bi. *Science* **350**, 413–416 (2015).
7. Q. Li, D. E. Kharzeev, C. Zhang, Y. Huang, I. Pletikosić, A. V. Fedorov, R. D. Zhong, J. A. Schneeloch, G. D. Gu, T. Valla, Chiral magnetic effect in $ZrTe_5$. *Nat. Phys.* **3648**, 550–554 (2016).
8. C.-L. Zhang, S.-Y. Xu, I. Belopolski, Z. Yuan, Z. Lin, B. Tong, G. Bian, N. Alidoust, C.-C. Lee, S.-M. Huang, T.-R. Chang, G. Chang, C.-H. Hsu, H.-T. Jeng, M. Neupane, D. S. Sanchez, H. Zheng, J. Wang, H. Lin, C. Zhang, H.-Z. Lu, S.-Q. Shen, T. Neupert, M. Z. Hasan, S. Jia, Signatures of the Adler-Bell-Jackiw chiral anomaly in a Weyl fermion semimetal. *Nat. Commun.* **7**, 10735 (2016).
9. S. A. Parameswaran, T. Grover, D. A. Abanin, D. A. Pesin, A. Vishwanath, Probing the chiral anomaly with nonlocal transport in three-dimensional topological semimetals. *Phys. Rev. X* **4**, 031035 (2014).
10. C.-Z. Li, L.-X. Wang, H. Liu, J. Wang, Z.-M. Liao, D.-P. Yu, Giant negative magnetoresistance induced by the chiral anomaly in individual Cd_3As_2 nanowires. *Nat. Commun.* **6**, 10137 (2015).
11. D. E. Kharzeev, J. Liao, S. A. Voloshin, G. Wang, Chiral magnetic and vortical effects in high-energy nuclear collisions—A status report. *Prog. Part. Nucl. Phys.* **88**, 1–28 (2016).
12. D. T. Son, A. R. Zhitnitsky, Quantum anomalies in dense matter. *Phys. Rev. D* **70**, 074018 (2004).
13. V. A. Zyuzin, Chiral electric separation effect in Weyl semimetals. *Phys. Rev. B* **98**, 165205 (2018).
14. Z. V. Khaidukov, V. P. Kirilin, A. V. Sadofyev, Chiral vortical effect in Fermi liquid. *Phys. Lett. B* **717**, 1–4 (2012).
15. P. Gallagher, C. -S. Yang, T. Lyu, F. Tian, R. Kou, H. Zhang, K. Watanabe, T. Taniguchi, F. Wang, Quantum-critical conductivity of the Dirac fluid in graphene. *Science* **364**, 158–162 (2019).
16. M. J. H. Ku, T. X. Zhou, Q. Li, Y. J. Shin, J. K. Shi, C. Burch, L. E. Anderson, A. T. Pierce, Y. Xie, A. Hamo, U. Vool, H. Zhang, F. Casola, T. Taniguchi, K. Watanabe, M. M. Fogler, P. Kim, A. Yacoby, R. L. Walsworth, Imaging viscous flow of the Dirac fluid in graphene. *Nature* **583**, 537–541 (2020).
17. C. Zhang, E. Zhang, W. Wang, Y. Liu, Z.-G. Chen, S. Lu, S. Liang, J. Cao, X. Yuan, L. Tang, Q. Li, C. Zhou, T. Gu, Y. Wu, J. Zou, F. Xiu, Room-temperature chiral charge pumping in Dirac semimetals. *Nat. Commun.* **8**, 13741 (2017).
18. F. Arnold, C. Shekhar, S. -C. Wu, Y. Sun, R. D. D. Reis, N. Kumar, M. Naumann, M. O. Ajeesh, M. Schmidt, A. G. Grushin, J. H. Bardarson, M. Baenitz, D. Sokolov, H. Borrmann, M. Nicklas, C. Felser, E. Hassinger, B. Yan, Negative magnetoresistance without well-defined chirality in the Weyl semimetal TaP. *Nat. Commun.* **7**, 11615 (2016).
19. J. Song, S. Kim, Y. Kim, H. Fu, J. Koo, Z. Wang, G. Lee, J. Lee, S. H. Oh, J. Bang, T. Matsushita, N. Wada, H. Ikegami, J. D. Denlinger, Y. H. Lee, B. Yan, Y. Kim, S. W. Kim, Coexistence of surface superconducting and three-dimensional topological Dirac states in semimetal KZnBi. *Phys. Rev. X* **11**, 021065 (2021).
20. B. Cheng, T. Schumann, S. Stemmer, N. P. Armitage, Probing charge pumping and relaxation of the chiral anomaly in a Dirac semimetal. *Sci. Adv.* **7**, eabg0914 (2021).
21. J. Song, B. C. Park, K. I. Sim, J. Bang, S. Kim, Z. Yang, Y. Kohama, Y. Kim, S. W. Kim, Tunable Berry curvature and transport crossover in topological Dirac semimetal KZnBi. *npj Quantum Mater.* **6**, 77 (2021).
22. M. Dressel, G. Grüner, *Electrodynamics of Solids* (Cambridge Univ. Press, 2003).
23. P. U. Jepsen, D. G. Cooke, M. Koch, Terahertz spectroscopy and imaging — Modern techniques and applications. *Laser Photon. Rev.* **5**, 124–166 (2011).
24. L. Wu, M. Brahlek, R. V. Aguilar, A. V. Stier, C. M. Morris, Y. Lubashevsky, L. S. Bilbro, N. Bansal, S. Oh, N. P. Armitage, A sudden collapse in the transport lifetime across the topological phase transition in $(Bi_{1-x}In_x)_2Se_3$. *Nat. Phys.* **9**, 410–414 (2013).
25. B. C. Park, T.-H. Kim, K. I. Sim, B. Kang, J. W. Kim, B. Cho, K.-H. Jeong, M.-H. Cho, J. H. Kim, Terahertz single conductance quantum and topological phase transitions in topological insulator Bi_2Se_3 ultrathin films. *Nat. Commun.* **6**, 6552 (2015).
26. J. D. Buron, D. H. Petersen, P. Bøggild, D. G. Cooke, M. Hilke, J. Sun, E. Whiteway, P. F. Nielsen, O. Hansen, A. Yurgens, P. U. Jepsen, Graphene conductance uniformity mapping. *Nano Lett.* **12**, 5074–5081 (2012).
27. H. Guerboukha, K. Nallappan, M. Skorobogatiy, Toward real-time terahertz imaging. *Adv. Opt. Photonics* **10**, 843–938 (2018).
28. C. J. Tabert, J. P. Carbotte, Optical conductivity of Weyl semimetals and signatures of the gapped semimetal phase transition. *Phys. Rev. B* **93**, 085442 (2016).
29. D. Rodriguez, A. A. Tsirlin, T. Biesner, T. Ueno, T. Takahashi, K. Kobayashi, M. Dressel, E. Uykur, Two linear regimes in optical conductivity of a type-I Weyl semimetal: The case of elemental tellurium. *Phys. Rev. Lett.* **124**, 136402 (2020).
30. B. -J. Yang, N. Nagaosa, Classification of stable three-dimensional Dirac semimetals with nontrivial topology. *Nat. Commun.* **5**, 4898 (2014).
31. L. Luo, D. Cheng, B. Song, L. -L. Wang, C. Vaswani, P. M. Lozano, G. Gu, C. Huang, R. H. J. Kim, Z. Liu, J. -M. Park, Y. Yao, K. Ho, I. E. Perakis, Q. Li, J. Wang, A light-induced phononic symmetry switch and giant dissipationless topological photocurrent in $ZrTe_5$. *Nat. Mater.* **20**, 329–334 (2021).
32. Q. Ma, S. -Y. Xu, C. -K. Chan, C. -L. Zhang, G. Chang, Y. Lin, W. Xie, T. Palacios, H. Lin, S. Jia, P. A. Lee, P. Jarillo-Herrero, N. Gedik, Direct optical detection of Weyl fermion chirality in a topological semimetal. *Nat. Phys.* **13**, 842–847 (2017).
33. G. B. Osterhoudt, L. K. Diebel, M. J. Gray, X. Yang, J. Stanco, X. Huang, B. Shen, N. Ni, P. J. W. Moll, Y. Ran, K. S. Burch, Colossal mid-infrared bulk photovoltaic effect in a type-I Weyl semimetal. *Nat. Mater.* **18**, 471–475 (2019).
34. S.-Y. Xu, N. Alidoust, I. Belopolski, Z. Yuan, G. Bian, T.-R. Chang, H. Zheng, V. Strokov, D. S. Sanchez, G. Chang, C. Zhang, D. Mou, Y. Wu, L. Huang, C.-C. Lee, S.-M. Huang, B. Wang, A. Bansil, H.-T. Jeng, T. Neupert, A. Kaminski, H. Lin, S. Jia, M. Z. Hasan, Discovery of a Weyl fermion state with Fermi arcs in niobium arsenide. *Nat. Phys.* **11**, 748–754 (2015).
35. S.-Y. Xu, I. Belopolski, D. S. Sanchez, C. Zhang, G. Chang, C. Guo, G. Bian, Z. Yuan, H. Lu, T.-R. Chang, P. P. Shibayev, M. L. Prokopovych, N. Alidoust, H. Zheng, C.-C. Lee, S.-M. Huang, R. Sankar, F. Chou, C.-H. Hsu, H.-T. Jeng, A. Bansil, T. Neupert, V. N. Strocov, H. Lin, S. Jia, M. Z. Hasan, Experimental discovery of a topological Weyl semimetal state in TaP. *Sci. Adv.* **1**, e1501092 (2015).
36. B. Q. Lv, H. M. Weng, B. B. Fu, X. P. Wang, H. Miao, J. Ma, P. Richard, X. C. Huang, L. X. Zhao, G. F. Chen, Z. Fang, X. Dai, T. Qian, H. Ding, Experimental discovery of Weyl semimetal TaAs. *Phys. Rev. X* **5**, 031013 (2015).

37. A. Damascelli, K. Schulte, D. van der Marel, Infrared spectroscopic study of phonons coupled to charge excitations in FeSi. *Phys. Rev. B* **55**, R4863(R) (1997).
38. Y. Zhao, H. Liu, C. Zhang, H. Wang, J. Wang, Z. Lin, Y. Xing, H. Lu, J. Liu, Y. Wang, S. M. Brombosz, Z. Xiao, S. Jia, X. C. Xie, J. Wang, Anisotropic fermi surface and quantum limit transport in high mobility three-dimensional Dirac semimetal Cd_3As_2. *Phys. Rev. X* **5**, 031037 (2015).
39. Y. Gao, S. Kaushik, E. J. Philip, Z. Li, Y. Qin, Y. P. Liu, W. L. Zhang, Y. L. Su, X. Chen, H. Weng, D. E. Kharzeev, M. K. Liu, J. Qi, Chiral terahertz wave emission from the Weyl semimetal TaAs. *Nat. Commun.* **11**, 720 (2020).
40. N. W. Ashcroft, N. D. Mermin, *Solid State Physics* (Brooks/Cole Publishing Company, 1976).
41. P. Rinkel, P. L. S. Lopes, I. Garate, Signatures of the chiral anomaly in phonon dynamics. *Phys. Rev. Lett.* **119**, 107401 (2017).
42. X. Yuan, C. Zhang, Y. Zhang, Z. Yan, T. Lyu, M. Zhang, Z. Li, C. Song, M. Zhao, P. Leng, M. Ozerov, X. Chen, N. Wang, Y. Shi, H. Yan, F. Xiu, The discovery of dynamic chiral anomaly in a Weyl semimetal NbAs. *Nat. Commun.* **11**, 1259 (2020).
43. A. Hui, Y. Zhang, E.-A. Kim, Optical signatures of the chiral anomaly in mirror-symmetric Weyl semimetals. *Phys. Rev. B* **100**, 085144 (2019).

Acknowledgments

Funding: This work was supported by the National Research Foundation of Korea (NRF) grant funded by the Korean government (Ministry of Science and ICT) (nos. 2021R1A6A1A03039696 and 2022R1A2C2004735), the Institute for Basic Science (IBS-R011-D1), and the Advanced Facility Center for Quantum Technology. B.C.P. acknowledges the support from the NRF grant funded by the Korean government (no. 2019R1A6A3A01096112). **Author contributions:** S.W.K. organized the project. B.C.P. grew the KZnBi single crystals. T.H. and B.C.P. conducted the THz experiments. T.S.J., B.C.P., and J.H.K. acquired the IR ellipsometry data. B.C.P., T.H., K.I.S., T.-T.K., Y.K., and Y.H.L. calculated and interpreted the THz mapping data. K.I.S., B.C.P., and T.H. designed a setup for angle-dependent magneto-THz measurements. B.C.P. and S.W.K. wrote the manuscript with the input of all authors. **Competing interests:** The authors declare that they have no competing interests. **Data and materials availability:** All data needed to evaluate the conclusions in the paper are present in the paper and/or the Supplementary Materials.

Submitted 28 March 2022
Accepted 7 October 2022
Published 25 November 2022
10.1126/sciadv.abq2479